

## Time-resolved microrheology of actively remodeling actomyosin networks

This content has been downloaded from IOPscience. Please scroll down to see the full text.

2014 New J. Phys. 16 075010

(<http://iopscience.iop.org/1367-2630/16/7/075010>)

View [the table of contents for this issue](#), or go to the [journal homepage](#) for more

Download details:

IP Address: 194.171.111.64

This content was downloaded on 21/07/2014 at 09:58

Please note that [terms and conditions apply](#).

## Time-resolved microrheology of actively remodeling actomyosin networks

Marina Soares e Silva<sup>1,3</sup>, Björn Stuhmann<sup>1,3</sup>, Timo Betz<sup>2</sup> and Gijsje H Koenderink<sup>1</sup>

<sup>1</sup>FOM Institute AMOLF, Science Park 104, 1098 XG Amsterdam, The Netherlands

<sup>2</sup>Institut Curie, Paris, France

E-mail: [g.koenderink@amolf.nl](mailto:g.koenderink@amolf.nl)

Received 21 March 2014, revised 26 May 2014

Accepted for publication 16 June 2014

Published 16 July 2014

*New Journal of Physics* **16** (2014) 075010

doi:[10.1088/1367-2630/16/7/075010](https://doi.org/10.1088/1367-2630/16/7/075010)

### Abstract


Living cells constitute an extraordinary state of matter since they are inherently out of thermal equilibrium due to internal metabolic processes. Indeed, measurements of particle motion in the cytoplasm of animal cells have revealed clear signatures of nonthermal fluctuations superposed on passive thermal motion. However, it has been difficult to pinpoint the exact molecular origin of this activity. Here, we employ time-resolved microrheology based on particle tracking to measure nonequilibrium fluctuations produced by myosin motor proteins in a minimal model system composed of purified actin filaments and myosin motors. We show that the motors generate spatially heterogeneous contractile fluctuations, which become less frequent with time as a consequence of motor-driven network remodeling. We analyze the particle tracking data on different length scales, combining particle image velocimetry, an ensemble analysis of the particle trajectories, and finally a kymograph analysis of individual particle trajectories to quantify the length and time scales associated with active particle displacements. All analyses show clear signatures of nonequilibrium activity: the particles exhibit random motion with an enhanced amplitude compared to passive samples, and they exhibit sporadic contractile fluctuations with ballistic motion over large (up to 30  $\mu\text{m}$ ) distances. This nonequilibrium activity diminishes with sample age,

<sup>3</sup> Equal contribution.



Content from this work may be used under the terms of the [Creative Commons Attribution 3.0 licence](https://creativecommons.org/licenses/by/3.0/). Any further distribution of this work must maintain attribution to the author(s) and the title of the work, journal citation and DOI.

even though the adenosine triphosphate level is held constant. We propose that network coarsening concentrates motors in large clusters and depletes them from the network, thus reducing the occurrence of contractile fluctuations. Our data provide valuable insight into the physical processes underlying stress generation within motor-driven actin networks and the analysis framework may prove useful for future microrheology studies in cells and model organisms.

 Online supplementary data available from [stacks.iop.org/NJP/16/075010/mmedia](https://stacks.iop.org/NJP/16/075010/mmedia)

Keywords: cytoskeleton, active soft matter, molecular motors

## 1. Introduction

Living cells are complex fluids that are constantly out of thermodynamic equilibrium as a result of dissipative processes in the cytoplasm [1–3], plasma membrane [4, 5] and nucleus [6, 7] fueled by metabolic energy. An important contributor to this internal activity in the cytoplasm of animal cells is the cytoskeleton, which is constantly remodeled by active (de-) polymerization of filamentous actin and microtubules and by motor proteins that slide these filaments or move cargo across them [8]. These processes cause active transport of cellular components that add to the ubiquitous thermal fluctuations that all cellular components are subject to due to their nano- to micro-scale dimensions [9]. Multiple studies have sought to quantify the departure of the cellular interior from thermal equilibrium by microrheometry [10]. Microrheometry is a miniaturized version of conventional rheometry that relies on tracking of colloidal probe particles. In studies of cells, the particles can either be embedded inside the cytoplasm or attached on the cell surface [11, 12]. The cytoplasm can be probed using endogenous particles, such as mitochondria or lipid granules, or using exogenous probes imported by microinjection or phagocytosis [13, 14]. Microspheres attached on the cell surface can be physically coupled to the intracellular actin cytoskeleton via transmembrane integrin receptors. There are two complementary microrheology methods [15]. Active microrheology probes the viscoelastic properties of a material by measuring the displacement of probe particles in response to an external force applied with optical or magnetic tweezers [16]. In contrast, passive microrheology probes the spontaneous displacements of beads embedded in a material in the absence of an external force [17, 18]. In thermal equilibrium, beads are subject only to thermal fluctuations, so the fluctuation-dissipation theorem (FDT) applies and passive microrheology measures the same response function as active microrheology [19]. The FDT is a generalization of Einstein’s description of Brownian motion of probe particles in a viscous liquid [20]. Any discrepancy between the response function measured by active versus passive microrheology provides evidence of nonequilibrium activity [21]. A few studies of cells combining passive and active microrheology have indeed demonstrated violations of the FDT due to intracellular activity at frequencies below a few Hz [22–25].

The exact microscopic origin of the observed nonequilibrium dynamics in cells is difficult to pinpoint due to their complex molecular composition and the complex architecture of the cytoskeleton [3, 26–31]. To circumvent this complexity, several studies have addressed

dynamics in minimal cytoskeletal model systems. Active (nonthermal) fluctuations have been observed both for actin networks activated by skeletal muscle myosin II motors [32–36] and in one recent study for nematic microtubule solutions activated by kinesins [37]. Myosin II is a motor protein with two heads that bind to actin filaments and uses chemical energy derived from hydrolysis of adenosine triphosphate (ATP) to generate pN-forces [38]. Individual myosin motors are non-processive, with a duty ratio of only a few per cent at saturating ATP levels. Nevertheless, single-headed myosin II subfragments have been shown to increase the effective temperature of actin networks [39]. Bipolar myosin II filaments, which resemble myosin minifilaments in cells, are more processive and can cause actin network contraction [40–43]. A combined active and passive microrheology study revealed clear violations of the FDT at low frequencies for active actin–myosin networks [33, 34]. Passive microrheology of these networks using video particle tracking revealed clear signatures of nonequilibrium activity in the particle fluctuations. Specifically, the distribution of displacements (or Van Hove correlations) showed a markedly non-Gaussian shape for spherical as well as rod-shaped probe particles [35, 36]. In spatially homogeneous networks, non-Gaussianity is indeed a signature of nonthermal activity [44, 45]. In crosslinked networks, myosin contractility can generate substantial contractile tension, which can stiffen actin networks by up to 100-fold [33, 46]. Recently, these nonequilibrium properties were successfully mimicked using noncytoskeletal components, in DNA gels activated by motors with processive DNA contraction activity [47]. All these experimental observations are well-accounted for by theoretical models that represent the myosin motor filaments as force dipoles in a homogeneous elastic medium [32, 48–50]. These models predict that the FDT is violated at frequencies below the inverse of the characteristic time scale of motor unbinding. The physical picture is that motors actively build up tension while bound to the actin network, which abruptly relaxes when the motors stochastically unbind [51]. This simple physical model inspired by experimental findings for *in vitro* actomyosin networks can, at least qualitatively, explain observations of nonequilibrium fluctuations observed in the cytoplasm of animal cells, although the exact contribution of myosin likely depends on cell type and on the location within the cytoplasm where fluctuations are probed [30].

An important complication in microrheology analysis of active networks is that myosin motors tend to cause substantial network remodeling. *In vitro* studies have shown that the length scale on which this remodeling occurs strongly depends on the presence of crosslinkers [40, 42, 43, 52, 53]. We recently showed that contractility in entangled actin networks containing myosin II motors is governed by a connectivity percolation criterion [54]. Above a threshold crosslink density corresponding to the percolation transition, the motors either macroscopically contract the network or they rupture it into disjoint clusters. In this regime, the motors remodel the network on a macroscopic length scale, hampering standard microrheology measurements. Below the percolation transition (i.e. below a threshold motor density), the myosin motors self-organize in dense clusters that contract only the adjacent actin network [41, 55]. In this regime, remodeling occurs only at a micrometer-length scale, so microrheology measurements are more straightforward [32, 33, 35, 36]. Nevertheless, one may anticipate time-dependent changes in the nonequilibrium fluctuations of embedded probe particles. In a recent study, we indeed obtained preliminary experimental evidence that myosin contractility causes network coarsening accompanied by a time-dependent reduction of nonequilibrium fluctuations [56].

Here, we employ time-resolved microrheology of actin–myosin networks at a crosslink density below the connectivity percolation threshold to investigate how nonequilibrium fluctuations evolve

during motor-driven network remodeling. We examine active networks in two distinct limits of motor density: at low motor density, the networks coarsen slowly and at small ( $\mu\text{m}$ ) scales, whereas at high motor density the networks coarsen fast and at larger ( $\sim 10\mu\text{m}$ ) scales. We find that contractile network coarsening causes the dynamics of the probe particles to be spatially heterogeneous, which complicates a standard particle tracking analysis. To address this challenge, we propose a multi-scale analysis of the data, combining particle image velocimetry (PIV), an ensemble analysis of the particle trajectories and finally a kymograph analysis of individual particle trajectories to quantify the time and length scales associated with active particle displacements. We find clear signatures of nonequilibrium activity in the ensemble-averaged dynamics, specifically enhanced (but still sub-diffusive) mean square displacements compared to passive control networks and strongly non-Gaussian displacement distributions. We show that these features reflect temporally heterogeneous particle motions, characterized by episodes of active, directed motion superposed on random motion. Our data provide valuable insight into the physical processes underlying stress generation within motor-driven actin networks and the analysis framework may prove useful for future microrheology studies in live cells and model organisms.

## 2. Materials and methods

### 2.1. Materials

Monomeric actin (G-actin) was purified from rabbit psoas skeletal muscle without column purification [57]. G-actin was stored at  $-80^\circ\text{C}$  in G-buffer (2 mM Tris-HCl, 0.2 mM  $\text{Na}_2\text{ATP}$ , 0.2 mM  $\text{CaCl}_2$ , 0.2 mM dithiothreitol (DTT), 0.5 mM  $\text{NaN}_3$ , pH 8.0). The actin concentration was determined by absorbance measurements at 290 nm using an extinction coefficient of  $1.1\text{ cm}^2\text{ mg}^{-1}$  [57]. Myosin II was also obtained from rabbit muscle and stored at  $-20^\circ\text{C}$  in a high salt buffer (0.6 mM KCl, 1 mM DTT, 50 mM phosphate, pH 6.3, 50% v/v glycerol) that prevents bipolar filament formation. Before experiments, myosin aliquots were dialyzed against 300 mM KCl, 4 mM  $\text{MgCl}_2$ , 1 mM DDT, 25 mM imidazole at pH 7.4. ( $\pm$ )Blebbistatin was obtained from Merck Chemicals (Nottingham, UK) and creatine phosphate and creatine kinase were from Roche Diagnostics (Almere, The Netherlands). Other chemicals were purchased from Sigma Aldrich. ATP was prepared as a 100 mM MgATP stock solution using equimolar amounts of  $\text{Na}_2\text{ATP}$  and  $\text{MgCl}_2$  in a 10 mM imidazole-HCl buffer (pH 7.4). Glass cells were assembled with a standard microscope slide and a  $24 \times 24\text{ mm}^2$  #1 coverslip (Menzel, Braunschweig, Germany) separated by two glass spacers ( $150\mu\text{m}$  height, cut from #1 coverslips), using optical adhesive Norland #81 (Edmund Optics, York, UK). We used polystyrene microspheres lot#GK0470701B (G Kisker Steinfurt, Germany), with a diameter of  $2\mu\text{m}$ . To prevent protein adsorption, the probe particles were passivated by adsorption of  $2 \times 10^{-8}\text{ mg PLL-PEG (PLL(20)-g[3.5]-PEG, SuSos, Switzerland)}$  per  $\mu\text{m}^2$  of particle surface. The positively charged PLL block adsorbs to the negatively charged microsphere surface, while the PEG block forms a brush layer that presents a steric barrier against protein adsorption.

### 2.2. Actomyosin network reconstitution

Actomyosin networks were prepared by mixing the proteins on ice in an assembly buffer of pH 7.4 with final concentrations of 25 mM imidazole-HCl, 50 mM KCl, 0.1 mM MgATP, 2 mM  $\text{MgCl}_2$ , 1 mM DTT, 2 mM trolox and an ATP regeneration mixture of 1.25 mM creatine

phosphate and 26 units mL<sup>-1</sup> creatine kinase. The actin concentration was always 1 mg mL<sup>-1</sup> (23.8 μM). We included crosslink points into the actin filaments by co-polymerizing biotinylated G-actin with unlabeled G-actin in a molar ratio of 1:1000. Excess streptavidin (streptavidin:actin molar ratio of 1:25) was included to form crosslinks between the biotinylated actin filaments. Streptavidin, combined with biotinylated G-actin monomers, forms a virtually permanent connection between actin filaments. Processive myosin bipolar filaments composed of ≈100 motors were pre-formed by fast dilution on ice of the myosin stock solution (in 300 mM KCl, 25 mM imidazole, 4 mM MgCl<sub>2</sub>, pH 7.4) with 25 mM imidazole buffer (pH 7.4) to low-salt (70 mM KCl). Myosin filaments were allowed to assemble for 5 min at room temperature. The molar ratio between myosin and actin was either 1:200 (*low motor density* regime) or 1:65 (*high motor density* regime). Polystyrene microspheres were added to actomyosin samples in a volume ratio of 1 to 2. Actomyosin network formation was initiated by adding monomeric G-actin and transferring the samples to glass flow cells and warming to room temperature. The flow cell surface was passivated with 0.1 mg mL<sup>-1</sup> κ-casein in assembly buffer to avoid non-specific interactions with the networks. The chambers were sealed with silicone grease to prevent solvent evaporation.

### 2.3. Particle tracking and data analysis

Particles embedded in actin–myosin or passive actin control networks were imaged in bright field on a Ti-Eclipse Nikon inverted microscope using a 40× oil immersion objective. Movies of 27 000 frames were recorded at a frame rate of 5 fps s<sup>-1</sup> and 12-bit starting 2 min after initiation of actin polymerization, using a Photometrics Coolsnap HQ2 digital CCD camera (Photometrics, Tucson, AZ, USA) controlled by NIS Elements AR 3.0 software (Nikon Instruments Europe BV, Amsterdam, The Netherlands). The exposure time was always 1 ms. The field of view was either 696×1040 pixels (half of the camera chip area) or 1392×1040 pixels (full size of the camera chip). Frames taken at reduced fields of view were not binned in space (pixel size 0.16 μm), while frames taken at larger field of view were 2× binned to reduce file size (pixel size 0.32 μm). Binning did not influence the accuracy of particle tracking, which was close to 20 nm, as checked by tracking beads immobilized on a coverslip. Raw data were stored as.nd2 files (Nikon format) and later converted to 16-bit tiff files for image processing. We imaged particles in the middle of the flow cell, to avoid any influence from the walls.

For PIV analysis, we used the MATLAB-based freeware PIVlab 1.32 written by William Thielicke (<http://pivlab.blogspot.nl/>). To create displacements between frames that are easily detectable, only every fifth image was utilized for PIV analysis, thus working with an effective frame rate of 1 s<sup>-1</sup>. All images were pre-processed using PIVlab's contrast-limited adaptive histogram equalization with a window size of 6.4 μm and a subsequent highpass filter with a window size of 2.9 μm. To retrieve frame-to-frame patch displacements we used PIVlab's direct cross-correlation algorithm with an interrogation window of 15 μm and an overlap between adjacent windows of 7.5 μm. Vectors with  $x$  or  $y$  component exceeding 1 μm s<sup>-1</sup> were found to persistently originate from erroneous detection and were hence discarded. We take for a given pair of frames the average of the magnitudes of all detected velocity vectors. We call this measure of coarse-grained network fluctuations the *frame-averaged velocity magnitude*,  $V_f$ . Before calculation of  $V_f$ , we de-drift the data by subtracting from each displacement vector the sum of all vectors of this frame. De-drifting eliminates overall network translation on the scale



of the field of view and thereby removes most of the externally induced fluctuations (albeit neither rotation nor divergence) as well as stage drift. We smoothed the time development of  $V_f$  using a box-car average with a time window of 100 s. In addition to  $V_f$ , velocity histograms were calculated at time intervals of 5 min by pooling all vector magnitudes detected within 1 min at the beginning of a 5 min period.

For ensemble mean square displacement analysis, individual particles were tracked using a custom-written algorithm implemented in C# (Microsoft.Net Framework 4.0, Redmond, USA) (see supplementary methods for details, available from [stacks.iop.org/NJP/16/075010/mmedia](http://stacks.iop.org/NJP/16/075010/mmedia)). Displacement data were de-drifted as described above for the PIV data. Ensemble mean square displacements at time intervals of 5 min were calculated using custom-built MATLAB routines, pooling all displacement values detected within a full 5 min period. Kymographs were made with the Kymograph plugin for ImageJ (<http://rsweb.nih.gov/ij/>) written by J Rietdorf (FMI Basel, Switzerland) and A Seitz (EMBL, Heidelberg, Germany).

### 3. Results

#### 3.1. Coarse-grained analysis of network dynamics by PIV

Active polymer networks were reconstituted by polymerizing globular (G-)actin in the presence of bipolar myosin II motor filaments. The networks had a constant (initial) mesh size of approximately 300 nm (corresponding to a fixed actin concentration of  $1 \text{ mg ml}^{-1}$ ) and constant average filament length ( $6 \mu\text{m}$ ) [41]. Under these conditions, the actin filaments form an entangled meshwork with the rheological response of a soft viscoelastic solid with an elastic modulus of 0.4 Pa that is five-fold larger than the viscous modulus (supplementary figure S1 (a)). We crosslinked the networks with a low density of permanent biotin–streptavidin crosslinks (on average two crosslinks per actin filament) that did not significantly change the shear modulus compared to that of uncrosslinked meshworks (figure S1(b)). Myosin was assembled into bipolar filaments with a mean length of  $0.69 \mu\text{m}$ , corresponding to about 100 myosin molecules per filament [41]. We tuned the contractile activity by varying the molar ratio between myosin and actin ( $R_M$ ) while keeping the ATP concentration fixed at 0.1 mM. At low myosin concentration ( $R_M = 1 : 200$ ), the networks slowly coarsened over a period of 60 min. The system evolved from an initially homogeneous meshwork with randomly dispersed myosin filaments to an inhomogeneous meshwork with dense myosin clusters surrounded by compact pockets of actin (figure S2(a)). The typical size of the actomyosin clusters was on the order of  $1 \mu\text{m}$ . In contrast, at high motor density ( $R_M = 1 : 65$ ), the myosin motors clustered together within 5 min and these clusters coalesced into larger superclusters within 15 min (figure S2(b)). These superclusters were tens of microns in size. We found by bulk rheometry that the motors increased the network stiffness by less than a factor of 2 (figure S1(b)), consistent with earlier findings showing that motors only generate substantial network stiffening at ultralow ( $\mu\text{M}$ ) ATP concentration [33] or at higher crosslink densities [46].

To probe the dynamics of the active networks, we co-polymerized actin and myosin in the presence of inert polystyrene microspheres with a diameter of  $2 \mu\text{m}$ . We found that a particle diameter  $2 \mu\text{m}$  was optimal for microrheology because the particles tended to stay uniformly distributed without excessive clustering (figure S3(a)). Smaller microspheres ( $1 \mu\text{m}$ ) were instead incorporated in clusters due to active network condensation, while larger particles ( $5 \mu\text{m}$ ) were insensitive to motor-driven network fluctuations. The particles are physically

trapped in the network and act as passive reporters of its dynamics. Even at 2 h after assembly, confocal fluorescence microscopy showed that there was no accumulation of either myosin or actin on the surface of the particles (figure S3(b)), confirming that the probes are inert reporters of the network dynamics. We observed the particles by bright field microscopy and recorded movies with a total duration of 90 min. We recorded four movies of independently prepared samples at  $R_M = 1 : 200$  and, in view of the larger spatial heterogeneity at higher motor density, six movies of independently prepared samples at  $R_M = 1 : 65$ . All movies are included in the analysis, but only a few representative movies are shown in the supplementary information.

At low motor density, the probe particles were homogeneously distributed in the network throughout the entire duration of the movies (figure 1(a) and movie S1). This is consistent with direct imaging of the network structure by confocal fluorescence microscopy, which showed that these networks coarsen only on  $\sim 1 \mu\text{m}$  length scales (figure S2(a)). In contrast, at high motor density we observed two different types of behavior. In three samples (coded s2a, s2g, s2h), the particles coalesced within 5 min into large clusters with sizes of 10–100  $\mu\text{m}$  (figure 1(b) labeled ‘fast’ and example movies S4 and S5). The time scale of this process is comparable to the time scale of myosin clustering observed by confocal microscopy (figure S2 (b)). It is therefore likely that the particles cluster because they are entrained with the network as it contracts. In the other three samples (s2b, s2c, s2d), we did not observe particle clustering (figure 1(b) labeled ‘slow’, example movies S2 and S3). This apparent sample-to-sample variability probably reflects spatial heterogeneity of the networks, given that for each sample we can only record a movie of one single field of view, which is limited to an area measuring  $225 \times 165 \mu\text{m}^2$  to ensure accurate particle tracking. Since high motor density samples exhibit motor-driven network coarsening on a scale of tens of  $\mu\text{m}$ , it is reasonable to expect different dynamics in different areas of the networks.

Given the difficulty of particle tracking in actively contracting networks, we decided to first analyze the contractile activity in a coarse-grained manner using PIV. PIV extracts the movements of features in the image on the spatial scale of an interrogation window. We chose an interrogation window of  $15 \mu\text{m}$ , corresponding to the typical distance between beads, with an overlap between adjacent windows of  $7.5 \mu\text{m}$ . In figure 1, velocity vectors from PIV analysis are overlaid on the still images taken near the beginning (2 min) and end (80 min) of the movies. The graphs show the corresponding distributions of the magnitudes of all detected velocity vectors, comparing active samples (blue symbols in figure 1(a) and red symbols in figure 1(b)) with passive samples (crossed circles in figures 1(a) and (b)). At early times, the active samples (open triangles in figures 1(a) and (b)) clearly exhibit larger velocities than passive samples (dark crossed circles). With increasing sample age, the velocity distribution measured for passive samples shifts somewhat to the left, perhaps because in the first 5 min the sample is still polymerizing (light crossed circles). For the active samples, the velocity distributions also shift to the left with increasing sample age. We observe two distinct types of dynamics. For samples that we will henceforth denote as *slow* samples, the velocity distribution shifts only slightly to the left, and the velocities measured after 90 min are still higher than in passive samples. This behavior is observed for the majority of samples at low motor density (three out of four data sets), and for three out of six data sets at high motor density. The velocity distributions measured for slow samples at low and high motor density are rather similar, but the late-time velocity distribution for the high motor density sample exhibits a pronounced shoulder, indicative of occasional large particle displacements. For samples that we will henceforth denote as *fast* samples, the velocities are larger than in *slow* samples at early times, but at late



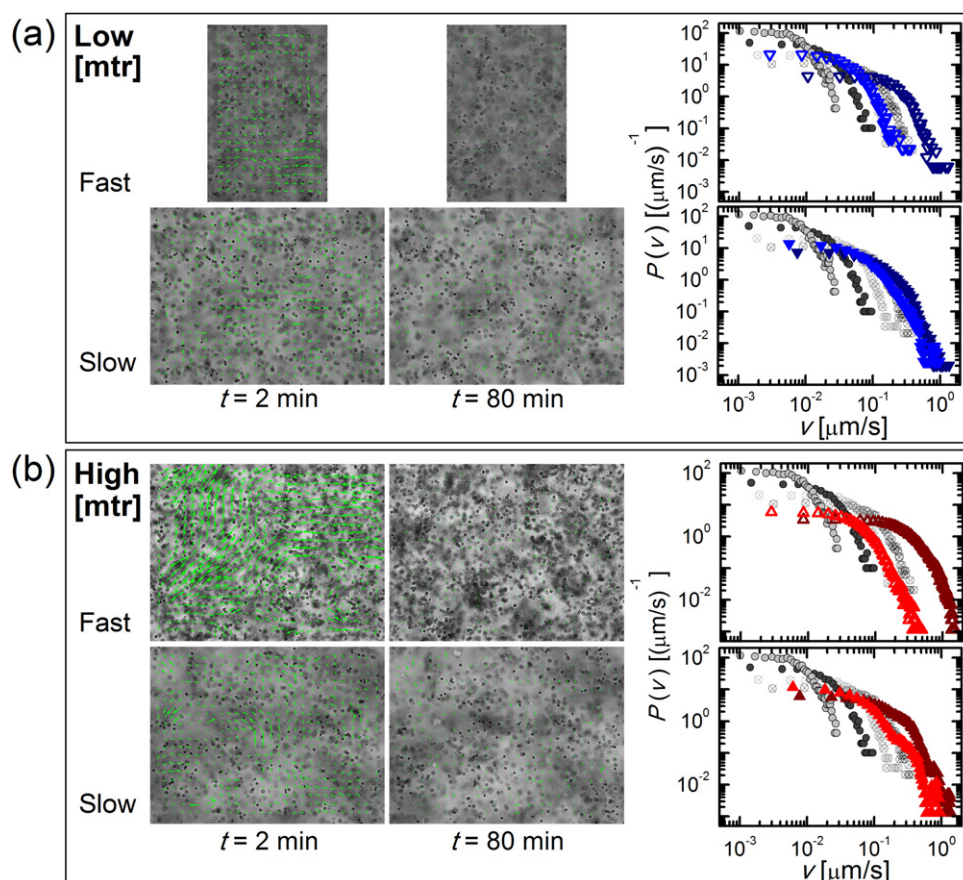


**Figure 1.** Particle image velocimetry (PIV) analysis of the contractile dynamics of actin–myosin networks seeded with spherical probe particles (visible as black dots), for (a) low motor density samples and (b) high motor density samples. Left: example bright field micrographs at early ( $t = 2 \text{ min}$ ) and late ( $t = 80 \text{ min}$ ) times, for samples classified as either *fast* or *slow* based on PIV analysis. Superposed in green are velocity vectors extracted with PIV. Scale: the height of each micrograph is  $170 \mu\text{m}$ . Right: corresponding velocity histograms (dark colored triangles:  $t = 2 \text{ min}$ ; bright colored triangles:  $t = 80 \text{ min}$ ). Crossed circles: passive sample without motors (dark gray:  $t = 2 \text{ min}$ ; light gray:  $t = 80 \text{ min}$ ). Solid circles: beads immobilized on a coverslip (dark gray:  $t = 2 \text{ min}$ ; light gray:  $t = 80 \text{ min}$ ). Datasets are averages of multiple data sets (see figure S4 for individual data sets).

times the velocities are smaller, and comparable to those measured in passive samples. In this case, no shoulder is present on the velocity histogram. Again, the velocity distributions at low and high motor densities are similar. The *fast* samples tend to show rapid clustering of the probe particles in the first 5 min as a consequence of network contraction (see movie S4), whereas the *slow* samples tend to have well-dispersed probe particles that do not significantly cluster (movies S1 and S2). It is important to note that the ATP concentration is maintained at a constant level by means of an enzymatic regeneration mixture. The apparent reduction of fluctuation activity with time is thus not due to depletion of ATP, but to motor-driven network remodeling.

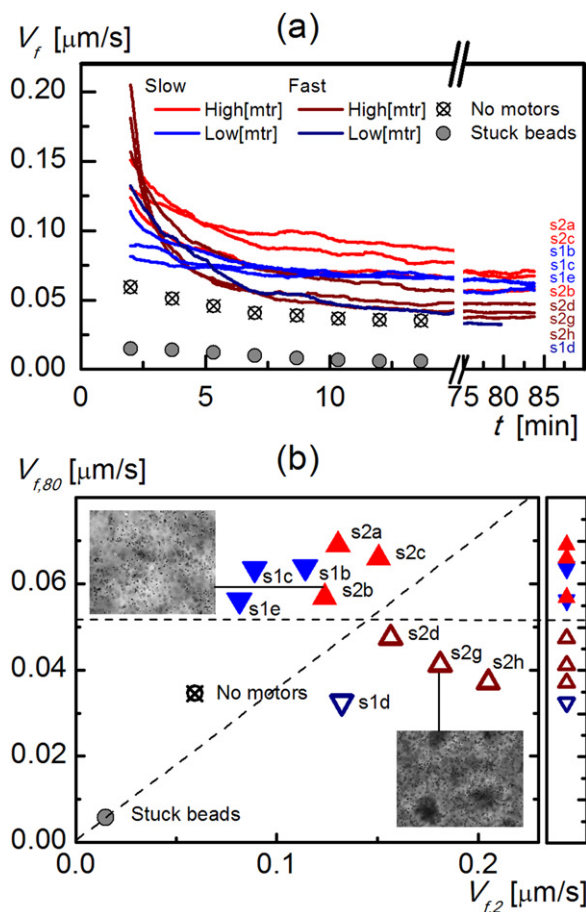


**Figure 2.** Time evolution of network dynamics according to PIV analysis. (a) Time evolution of frame-averaged velocity magnitude for each data set. Color code: red curves correspond to high motor density samples and blue curves to low motor density samples (see legend). (b) Correlation between early-time ( $t=2$  min) and late-time ( $t=80$  min) frame-averaged velocity magnitudes plotted for all individual movies. Blue solid triangles (samples s1b, s1c, s1d, s1e):  $R_M = 1:200$ . Red solid triangles (samples s2a, s2b, s2c):  $R_M = 1:65$ , slow coarsening. Red open triangles (samples s2d, s2g, s2h):  $R_M = 1:65$ , fast coarsening. Insets: bright field micrographs show typical late-time bead distributions of *slow samples* (above horizontal dashed line) and *fast samples* (below horizontal dashed line).

The velocity distributions obtained from PIV analysis exhibit a marked dependence on sample age. To quantify this effect more systematically for all data sets (see figure S4 for complete overview), we calculate the average value of the magnitudes of all velocity vectors between sequential frames, which we denote as the frame-averaged velocity magnitude,  $V_f$ . As shown in figure 2(a),  $V_f$  for all samples decreases monotonically with sample age, reaching a steady state value after 20 min (determined as the time point where 90% of the  $V_f$  drop has occurred, mean of all samples). Interestingly, samples that have an initially high  $V_f$  have a small final  $V_f$ , whereas samples that have an initially low  $V_f$  have a larger final  $V_f$ . This inverse correlation between early- and late-time velocity is summarized in figure 2(b), where the diagonal line indicates a ratio of the velocities at  $t=2$  min and  $t=80$  min corresponding to  $V_{t=2}/V_{t=80} = 2.75$ . Samples below the

diagonal line are the ones that we denote as *fast* samples, since they display fast dynamics in the first few minutes of sample evolution. In this category, we find three data sets of high motor density samples and one movie of a low motor density sample. The particle distribution in these samples at late times tends to be inhomogeneous with large clusters (inset of figure 2(b) and figure S3(c)). Samples above the diagonal line show a moderate decline of  $V_f$  and correspond to the ones that we term *slow* samples. In this category, we find three data sets of high motor density samples and three data sets of low motor density samples. Nearly all slow samples (except for sample s2a) display homogeneous late-time bead distributions (see inset of figure 2(b)). The horizontal line in figure 2(b) distinguishes the samples by their late-time ( $t=80$  min)  $V_f$ , creating the same classification as the diagonal line into *fast* samples (low  $V_f$ ) and *slow* samples (higher  $V_f$ ).

### 3.2. Microscopic analysis of network dynamics by ensemble-averaged particle trajectories

To examine network dynamics on a smaller length scale, corresponding to the scale of the embedded probe particles, we tracked the particle centroid positions with sub-pixel accuracy [58]. Tracking of *fast* samples with initially high  $V_f$  was possible only after  $t=7$  min, because of the rapid particle clustering and accompanying rapid changes in pixel intensities of the particles at early times. Tracking of *slow* samples was possible for the entire experiment duration. To resolve the time evolution of the dynamics, we divided the entire 90 min of each movie into bins of 5 min.

Figure 3(a) shows ensemble-averaged distributions of particle displacements (left; at a lag time  $\tau=10$  s), while figure 3(b) shows the corresponding distributions for high motor concentration samples. In both cases, we separated data sets measured for *fast* versus *slow* samples (see legend on the left). For reference, the displacement distributions measured for passive samples are shown as small crossed circles. For the passive samples, the displacement distributions are well-described by Gaussian functions (dashed lines), indicating that the networks are homogeneous [44]. In contrast, the active samples exhibit displacement distributions with pronounced non-Gaussian tails. The central part of the distributions can still be fitted by a Gaussian function (solid lines), but the width of the Gaussian is larger than for the passive samples. Similar distributions have been observed previously by Toyota and coworkers [35] for  $1\ \mu\text{m}$  silica particles embedded in crosslinked actin–myosin networks. It was argued there that the central Gaussian part of the distribution represents a superposition of random thermal motion and of active fluctuations caused by many independent motors far from the probe particles, whereas the tails of the distribution reflect rare events associated with force generation by only a few (or even a single) motors in close proximity to the probe particles. As the sample age increases from 10 to 80 min, we observe that both the width of the central Gaussian portion and the contribution of the non-Gaussian tails decrease. Consistent with PIV analysis, the displacement distributions thus also indicate an apparent reduction of activity over time. The time evolution is similar for all samples, independent of motor density. *Slow* samples exhibit somewhat larger tails in the displacement distributions than *fast* samples (further quantified below).

The ensemble-averaged mean square displacements for samples of low motor density (figure 3(a), right) and high motor density (figure 3(b), right) reveal a similar evolution with sample age: in young samples ( $t=10$  min) the mean square displacement is large and increases almost linearly with lag time, whereas at  $t=30$  min the mean square displacement has dropped substantially and increases with a smaller power law in lag time. At low motor density, there is

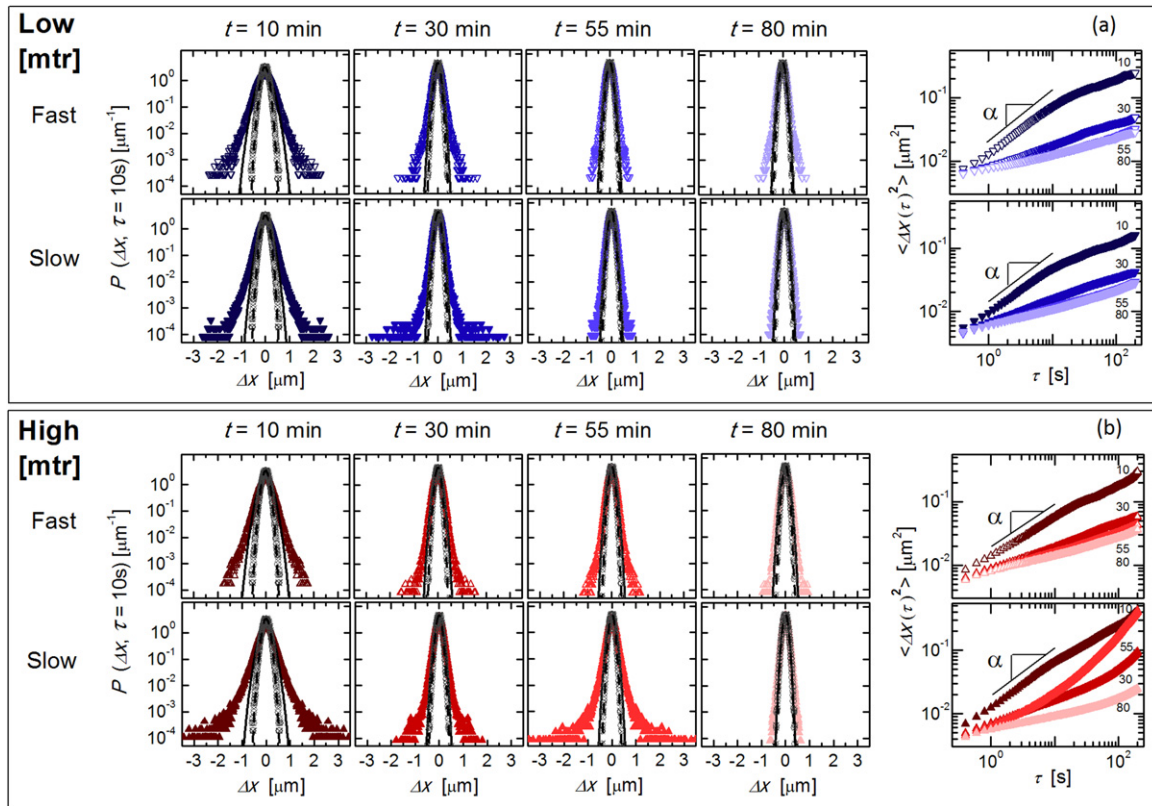


**Figure 3.** Ensemble particle trajectory analysis for (a) low motor density samples and (b) high motor density samples. Left: step width distributions (Van Hove correlations) at a lag time  $\tau = 10$  s for different sample ages (see legend on top of the graphs), shown separately for *fast samples* versus *slow samples* (see legend on the left). Small crossed circles: passive sample without motors. Solid (dashed) line: Gaussian fit to active (passive) data. Right: corresponding mean square displacements in the  $x$ -direction, with sample ages indicated as numbers (in minutes) next to the curves. The solid lines with slope  $\alpha$  show examples of power-law fits to the curves measured at  $t=0$ , which are used to determine the diffusive exponent  $\alpha$ .

no immediately apparent difference between *slow* and *fast* samples. At high motor density, however, *slow* samples apparently take a longer time to ‘age’, showing a larger mean square displacement up to  $t=55$  min and also larger tails in the displacement distributions compared to *fast* samples.

To summarize the evolution of the dynamics with sample age, we extract several dynamic parameters from the ensemble-averaged displacement distributions and mean square displacements for each movie (see figure S5). The first parameter is the apparent diffusive exponent,  $\alpha$ , which we obtain as the slope of a power-law fit to the mean square displacement for lag times  $\tau$  between 1 and 8 s (indicated by solid lines in figures 3(a), (b)). In all samples, irrespective of motor concentration or dynamic regime,  $\alpha$  is initially close to 0.9 and then decreases to a steady state value of around 0.25 (figure 4, panel labeled ‘ $\alpha$ ’). The time scale for  $\alpha$  to drop by 90% is 45 min (mean of all samples). Once the samples reach a steady state,  $\alpha$  is comparable for active and passive (crossed circles) samples. The second parameter is the Gaussian broadening,  $\beta$ , which we define as the width of the central portion of the displacement



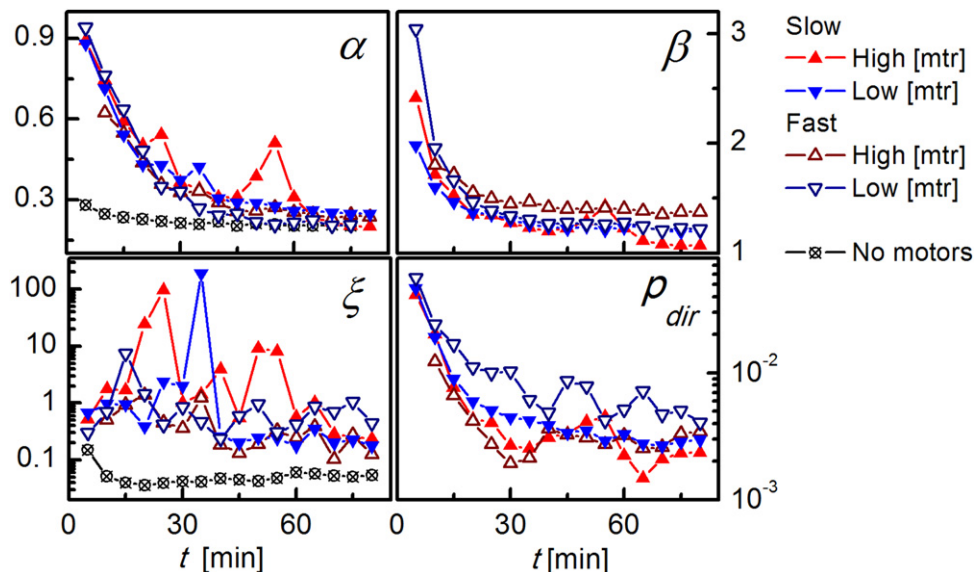


**Figure 4.** Different measures of nonequilibrium activity extracted from particle tracking analysis plotted as a function of sample age. Measures (see legends in the corner of each panel) are the diffusive coefficient  $\alpha$ , the Gaussian standard deviation ratio  $\beta$ , the non-Gaussian parameter  $\xi$  at a lag time of 10 s and the probability for a particle to undergo directed motion  $\rho_{dir}$ . As indicated in the legend on the right, data have been pooled according to motor concentration (red symbols = high, blue = low) and dynamics regime (bright filled symbols = *slow samples*, dark open symbols = *fast samples*). Crossed circles: passive control sample. The corresponding individual data sets are shown in figure S4.

distribution of active samples divided by the width of the Gaussian distribution of passive samples. As shown in figure 4 (panel labeled ' $\beta$ '),  $\beta$  decreases monotonically with sample age over a time period of about 45 min. The third parameter is the non-Gaussian parameter [35],

$$\xi = \frac{\langle \Delta x(\tau)^4 \rangle}{3 \langle \Delta x(\tau)^2 \rangle^2} - 1, \quad (1)$$

which quantifies the degree of non-Gaussianity of the displacement distributions, taking a value of zero for a perfectly Gaussian distribution. For passive control samples (crossed circles in figure 4, panel labeled ' $\xi$ '),  $\xi$  is initially 0.15 and decreases to a steady state value of 0.05 within 15 min, close to zero, as expected for a homogeneous polymer network [44]. For the *slow* samples (solid triangles), both at low and high motor density,  $\xi$  is substantially larger than for the passive control samples and exhibits large fluctuations, taking values between 0.2 and 200. At low motor density, these large fluctuations continue until  $t=45$  min, while at high motor density the large fluctuations persist until  $t=60$  min. In steady state,  $\xi$  is close to 0.2 at both low and high motor density, which is still substantially higher than  $\xi$  of passive samples. The large fluctuations in  $\xi$  reflect the fact that the non-Gaussian tails represent rare events associated with force generation by single motors close to the probe particles [35, 56]. For the *fast* samples (open triangles), both at low and at high motor density,  $\xi$  fluctuates less than for *slow* samples and does not show a clear dependence on sample age. Over the entire time window,  $\xi$  is about an order of magnitude larger than for passive samples.

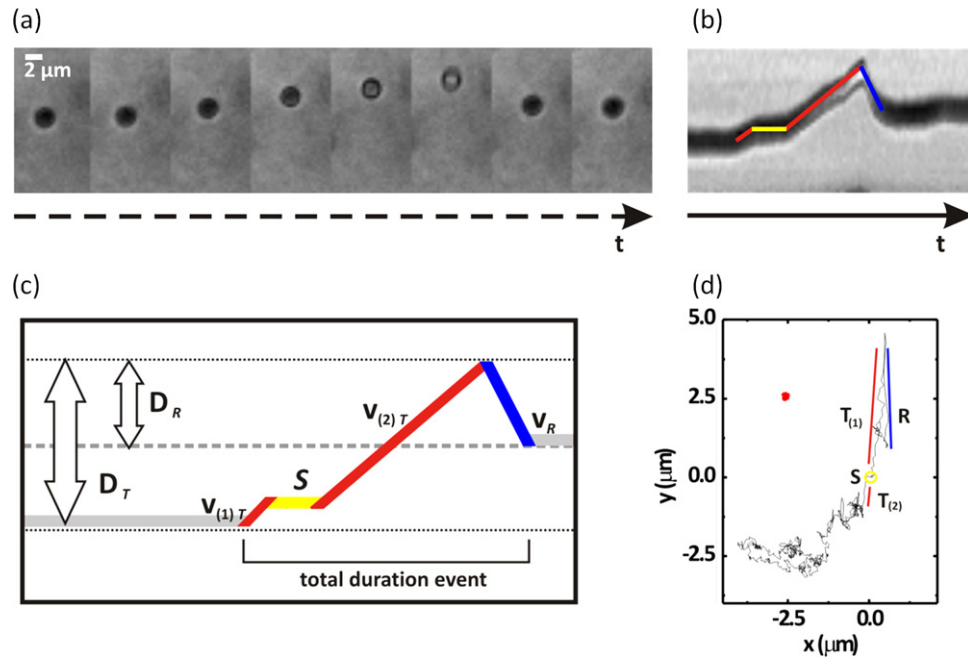


**Figure 5.** Kymograph analysis of active contractile fluctuations of individual probe particles in active networks. (a) Time sequence showing a particle exhibiting a contractile fluctuation consisting of a translocation followed by reversal. Scale bar is  $2\ \mu\text{m}$ . (b) Corresponding kymograph projection along the direction of particle translocation. The contractile fluctuation is clearly distinguishable from the baseline random fluctuations. (c) The contractile fluctuation can be dissected into a translocation (in red) over a distance  $D_T$  with velocity  $\nu_T$ ; a reversal (in blue) over a distance  $D_R$  with velocity  $\nu_R$ ; and a stationary period (in yellow) of duration  $S$ . (d)  $x$ - $y$  trajectory of a probe particle showing a combination of random motion (dense part of the trajectory within the yellow circle) and large-amplitude motor-driven fluctuations (red and blue guiding lines). Inset (in red): trajectory of a probe particle in a passive control network.

We have shown previously that the non-Gaussian tails in the displacement distributions for probe particles embedded in actomyosin networks originate from sporadic, large-amplitude contractile fluctuations [56]. In order to distinguish these directed motion events from the otherwise apparently random motion, we used a segmentation algorithm that provides the probability of a particle (per unit of time) to show directed motion,  $p_{\text{dir}}$  [56] (figure S6 and movie S6). As shown in figure 4 (panel labeled ' $p_{\text{dir}}$ '), this fourth dynamic parameter also decreases with sample age for all samples, from an initial value of  $\sim 0.04$  to a final value of  $\sim 0.003$  (average over all samples). Surprisingly,  $p_{\text{dir}}$  is largest in the *fast* sample at low motor density.

### 3.3. Microscopic analysis of network dynamics by single-particle trajectory analysis

Single particle trajectories in active networks were characterized by long periods of small-amplitude random motion interrupted by short episodes of large-amplitude directed motion (figure 5(d)). This motion is clearly distinct from the small-amplitude random motion seen in passive control networks (red trajectory shown as an inset in figure 5(d)). To characterize the time and length scales associated with directed motion, we analyzed individual events by



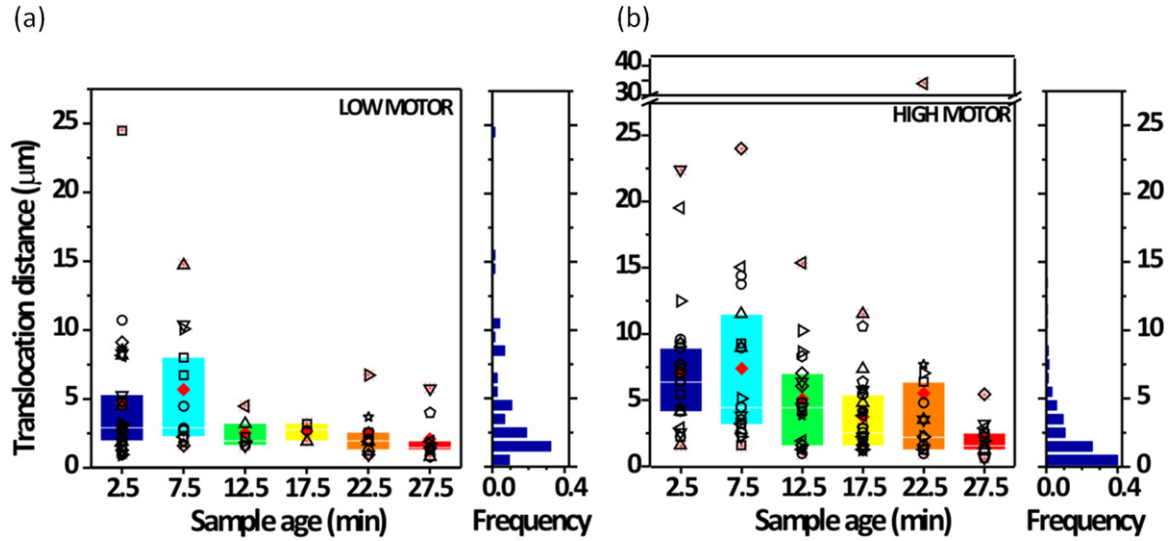


**Figure 6.** Sample-age dependence of the distance ( $D_T$  in figure 5(c)) over which individual particles are translocated during contractile fluctuation events at (a) low motor density and (b) at high motor density. Graphs show individual data points, and colored box plots represent 25th–75th percentile of data with sample age incrementing towards hot colors. Histograms on the right hand side of the graphs show lumped distributions of translocation distances.

producing kymographs, which are space–time plots along the direction of motion (see image sequence in figure 5(a) and corresponding kymograph in figure 5(b)). The kymographs reveal directed displacements, which are clearly distinguishable in amplitude from the baseline random motion. The example shows a particle that suddenly moves in a ballistic manner (indicated by red lines), experiencing a short stationary period (indicated by yellow line), and then abruptly moves back towards its original position (indicated by blue line). To quantify the distances and velocities associated with particle motion, we divide the kymographs into translocation events (over a distance  $D_T$  and with velocity  $\nu_T$ ) and reversal events (over a distance  $D_R$  and with velocity  $\nu_R$ ), as shown in figure 5(c). Some particles exhibited repeated contractile fluctuations separated by pauses, both at low motor density (figure S7(a)) and high motor density (figure S7(b)). We also noticed that pairs of particles sometimes exhibited anti-correlated motion, likely caused by a motor located inbetween the two particles (figure S7(c)). In some cases, multiple particles exhibited simultaneous fluctuations in the same direction (figure S7(d)). Since these events were rare, we did not attempt to quantify them.

As shown in figure 6(a) (low motor density) and (b) (high motor density), the displacements of particles during translocation events ( $D_T$ ) ranged from a few hundred nm to 30  $\mu\text{m}$ . Since both PIV analysis and the ensemble-averaged dynamics showed an evolution of apparent activity with sample age, we analyzed the time dependence of translocation distances. Large displacements ( $>7 \mu\text{m}$ ) occurred only at early times, up to  $t = 10$  min in low motor density samples and up to  $t = 20$  min in high motor density samples. At later times, the displacements were limited to at most 7  $\mu\text{m}$ . The average translocation distance was similar at low and high motor density, 3.8  $\mu\text{m}$  ( $N = 71$ ) and 4.6  $\mu\text{m}$  ( $N = 192$ ), respectively. The translocation speeds showed a broad range of values, from 0.2 to 4  $\mu\text{m s}^{-1}$ . On average, the translocation speed was somewhat lower in low motor density samples (0.8  $\mu\text{m s}^{-1}$  ( $N = 142$ ), figure S8(a)) compared to

high motor density samples ( $1.1 \mu\text{m s}^{-1}$  ( $N=187$ ), figure S8(b)). The order of magnitude of the velocities is consistent with the unloaded translocation speed of  $\sim 5 \mu\text{m s}^{-1}$  observed for actin filaments on myosin-coated substrates in motility assays [59]. The speeds are also comparable to the velocity magnitudes obtained by PIV analysis (figure 1). The speed during reversals was also broadly distributed, and was on average slightly higher than the speed during translocations ( $1 \mu\text{m s}^{-1}$  at low motor density ( $N=103$ ), figure S8(a);  $1.7 \mu\text{m s}^{-1}$  at high motor density ( $N=157$ ), figure S8(d)).

Given that the translocation distances are often many times larger than the mesh size (300 nm), the question arises how reversible the particle displacements are. To quantify reversibility, we determined the distance covered during translocation ( $D_T$ ) and reversal ( $D_R$ ) in kymographs (see figure 6(a)) and define the percentage of return of a probe to its initial position after a translocation as  $D_R/D_T \times 100\%$ . As shown in the histograms in figures 7(b) and (c), only a small percentage (10–15%) of particles returned to their original position, while about 50% made an incomplete recovery and a small percentage (15% at low motor density, 20% at high motor density) did not recover at all. On average, reversibility was somewhat higher in low motor density samples than high density samples (average per cent return 71% at low motor density ( $N=72$ ) and 56% at high motor density ( $N=188$ )). Interestingly, a significant fraction (14%) of the particles moved back further than their original translocated distance. These events are suggestive of reversals by an active, motor-dependent mechanism. In the case of passive network relaxation, one expects either full recovery (for a purely elastic deformation) or incomplete recovery (in case of plastic network deformation).

Since we observed clear evidence of network plasticity in the form of irreversible translocations, we tested whether the per cent recovery was correlated with the distance over which probe particles moved during a translocation event. As shown in figures 7(b) (low motor density) and (c) (high motor density), the percentage of return of the probes to their initial position indeed showed a significant inverse correlation with translocation distance (correlation coefficient  $R = -0.6$ ,  $p = 4 \times 10^{-7}$ ). Large particle displacements, which occur mostly during the first 10 min after sample preparation, thus tend to be more irreversible.

#### 4. Discussion

We used time-resolved microrheology of an *in vitro* model system based on purified actin and myosin II to resolve how motor-driven network remodeling influences the athermal fluctuations of embedded probe particles. We examined active networks of entangled actin filaments at a crosslink density below the connectivity percolation threshold. In this regime, the myosin motors self-organize in dense clusters that contract the adjacent actin network on a local (micrometer) length scale [41, 54]. We investigated two limits of motor density, which differ in the time and length scale associated with network remodeling. Confocal imaging showed that at high motor density ( $R_M = 1 : 65$ ), the motors cause fast network coarsening (5–10 min) into clusters with sizes of tens of  $\mu\text{m}$ , whereas at low motor density ( $R_M = 1 : 200$ ), the networks coarsen more slowly (30 min) and at a smaller (micrometer) scale. We find that network coarsening causes the dynamics of the embedded probe particles to be spatially and temporally heterogeneous, complicating a standard particle tracking analysis. To address this challenge, we performed a multi-scale analysis of the data.

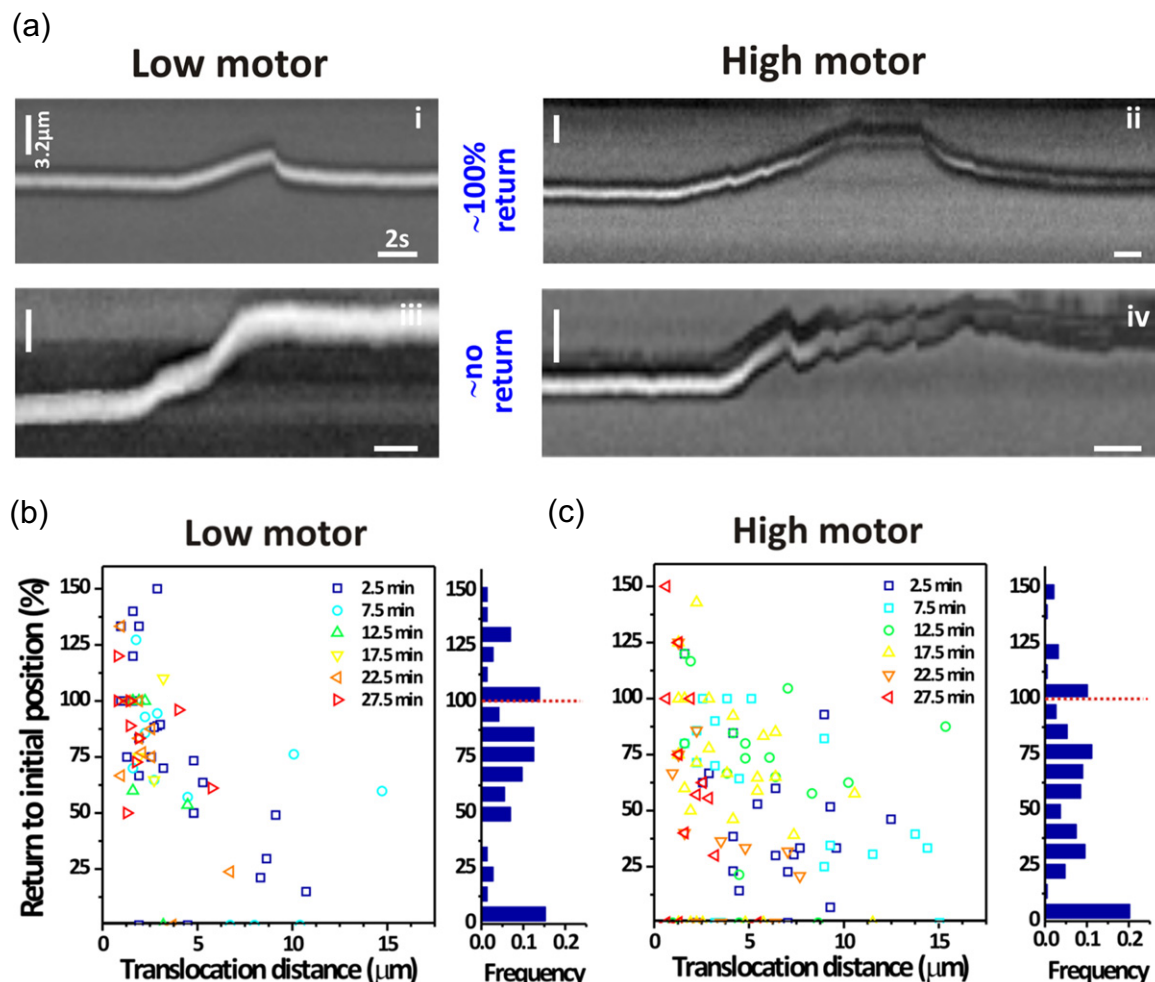


**Figure 7.** Reversibility of particle translations. (a) Examples of a probe particle exhibiting a single translocation-reversal event with either complete (i), (ii) or incomplete (iii), (iv) reversal. (b) Correlation between the degree of reversibility and the distance of particle translocation in samples of low motor density. (c) Correlation between the degree of reversibility and the distance of particle translocation in samples of high motor density. The colors correspond to different sample ages (see legend), with gradient from cold (2.5 min) to warm (27.5 min) color. The largest ( $>5 \mu\text{m}$ ) and more irreversible displacements take place during the first 10 min. Irreversibility is greater at high motor density than at low motor density. Histograms on the right hand side of the graphs show lumped distributions of percentage of return. A return percentage ( $D_T/D_T \times 100\%$ ) of 100% corresponds to full reversibility, 0% to irreversibility and  $>100\%$  to overshoot beyond the original position.

A coarse-grained analysis by PIV with an interrogation window size of  $15 \mu\text{m}$  revealed that all samples display a drop in the amplitude of large-scale active fluctuations within 20 min. Furthermore, PIV analysis demonstrated variable dynamics among independently prepared samples of the same composition. This heterogeneity was particularly pronounced at high motor density. In *slow* samples, the beads remained homogeneously distributed and the frame-averaged velocity decreased only moderately (approximately two-fold). In contrast, *fast* samples exhibited rapid particle clustering indicative of network contraction within 5–10 min

and the frame-averaged velocity started higher but ended lower than in *slow* samples (approximately four-fold decrease of  $V_f$ ). We suspect that this variability reflects not so much a difference between samples, but rather the spatial heterogeneity of the samples, which is especially pronounced for high motor density samples. To ensure accurate particle tracking, we had to record movies of relatively small fields of view ( $225 \times 165 \mu\text{m}^2$ ), and because the samples evolved over time we could only record one movie for each sample. This is an inherent technical limitation of particle tracking microrheology of spatially heterogeneous samples. In future, it will be interesting to combine particle tracking with concurrent confocal imaging of the network structure. Instead of tracer particles, it should also be possible to directly track either actin structures [60, 61] or myosin foci [62].

To quantify network fluctuations on a smaller spatial scale ( $2 \mu\text{m}$ ), we performed a complementary analysis of the individual particle trajectories. The trajectories exhibited clear signatures of nonequilibrium activity, with sporadic contractile fluctuations. These fluctuations comprised directed motion over a large (up to  $30 \mu\text{m}$ ) distance followed by (usually partial) reversal. The ensemble-averaged displacement distributions of the particles exhibited prominent non-Gaussian tails, which originate from these sporadic athermal fluctuations caused by motors in close proximity of the particles. Additionally, the displacement distributions had a Gaussian central portion with a width that was larger than the width of the Gaussian displacement distributions observed for passive samples. This widening reflects active force generation by many independent motors far from the probe particles [35].

Consistent with the PIV analysis, the particle trajectories also showed a clear reduction of athermal fluctuations with increasing sample age: the diffusive exponent decreased, the non-Gaussian parameter decreased, the width of the Gaussian central part of the displacement distributions decreased and kymograph analysis revealed smaller translocation distances during contractile fluctuations. Automated trajectory segmentation showed that active fluctuations are more and more infrequent at late times. The decay time for the reduction of apparent activity was 20 min according to the frame-averaged velocity determined by coarse-grained PIV analysis, which is shorter than the decay time observed for the dynamic parameters measured with particle tracking ( $\alpha$ ,  $\beta$ ,  $\xi$ ,  $P_{\text{dir}}$ ). This difference in decay times indicates that PIV is less sensitive to residual active fluctuations than particle tracking, which is reasonable since PIV averages over all image features and also has a smaller spatial resolution.

In steady state, the samples did retain clear signs of residual activity: the non-Gaussian parameter was still about ten-fold larger than for passive samples and we still detected active contractile fluctuations. Indeed, the ATP concentration in the samples was kept at a constant level by an enzymatic regeneration mixture. Thus, the apparent reduction of activity over time is not due to ATP depletion. Instead, confocal imaging of the network structure over time indicates that the reduction of activity is caused by contractile coarsening. We speculate that motor filament clustering and local network contraction concentrate motors within dense clusters that are shielded from the surrounding network by a dense actin shell. At the same time, myosin motors are depleted from the network, resulting in low residual active fluctuations in the network once the network structure has reached a steady state. Both PIV analysis and particle tracking analysis indicated that *slow* samples (or sample regions) have larger residual activity in steady state than *fast* samples. We speculate that the residual activity in *fast* samples is lower because they show more rapid and extensive motor clustering. At high motor density, contractile coarsening was more rapid and occurred on a larger scale than in slow samples, explaining why the dynamics was more heterogeneous. Contractile fluctuations in the first

10 min, which network remodeling occurred, involved large (up to  $30\ \mu\text{m}$ ) particle displacements, accompanied by irreversible network remodeling.

Previous experimental [33–35] and theoretical studies [48, 50] interpreted probe particle dynamics in contractile actin–myosin networks based on the assumption of a homogeneous elastic medium. Our findings demonstrate that active networks are spatially and temporally heterogeneous and exhibit plastic deformation. Video particle tracking microrheology can provide insight into the length and time scales associated with network remodeling. Previous *in vitro* studies of myosin-driven remodeling of actin networks have revealed a rich phase space tuned by motor activity (i.e. by motor density, ATP concentration and ionic strength) and network connectivity (i.e. by crosslink density, actin filament density and actin filament length). Low crosslink densities as used in this study promote micrometer-scale network contraction and transient build-up of stress. In the absence of crosslinks, motor activity has instead been shown to cause network fluidization [63]. In dilute solutions of bundled actin filaments (below  $0.3\ \text{mg ml}^{-1}$  actin), motor activity has been shown to cause superdiffusive motion of the bundles [60, 61], as opposed to the sub-diffusive dynamics observed in the entangled networks studied here. At high enough crosslink and motor density, motor activity can cause large-scale formation of ordered patterns [52], large-scale network contraction [40, 42, 43, 54], or strong network stiffening [33, 46]. It will be interesting to apply the microrheology analysis developed in this paper to different regimes in this complex phase space, to elucidate the role of motor activity and network connectivity in controlling nonequilibrium fluctuations.

## 5. Conclusion

We used time-resolved microrheology to investigate the dynamics of active actin–myosin networks at low crosslink density. We showed that the motors generate spatially heterogeneous network fluctuations that evolve over time due to motor-driven contractile coarsening. At larger motor density ( $R_M = 1 : 65$ ) the dynamics was more heterogeneous than at lower motor density ( $R_M = 1 : 200$ ). Since the inhomogeneous dynamics hampers a standard single-particle tracking analysis, we analyzed the particle tracking data on different scales. A coarse-grained analysis by PIV revealed that motors locally compact the actin network, which is accompanied by decreasing apparent activity over time. We propose that network coarsening, which concentrates motors in large clusters, depletes motors from the network and thus reduces the occurrence of contractile fluctuations. If a network region evades excessive coarsening, it will retain a larger residual activity. An ensemble analysis of the particle displacements revealed that motor activity causes a strongly enhanced mean square displacement compared to that in passive samples. Moreover, motor activity resulted in a non-Gaussian displacement distribution. Consistent with the PIV analysis, the particle trajectory analysis also revealed reduced activity with increasing sample age. Finally, a kymograph analysis of individual particle trajectories revealed that the particles exhibit intermittent contractile fluctuations. The particles exhibited rather large displacements of up to  $30\ \mu\text{m}$ , especially during the first phase of network remodeling. There was clear evidence of network plasticity, since particle translocations were usually not completely reversible. Our findings show that networks of entangled actin filaments with embedded myosin motors are spatially and temporally heterogeneous. It will be interesting to compare these findings to the dynamics of actin–myosin networks in the cortex of living cells and embryos, where pulsatile network contractions have been observed [64].



## Acknowledgments

This work is part of the research program of the Foundation for Fundamental Research on Matter, which is financially supported by the Netherlands Organization for Scientific Research (NWO). The work was funded in part by an NWO VIDI grant and an HFSP Young Investigator grant of the International Human Frontier Science Program Organization. We thank Marco Seynen for writing the *BeadTracker* software and Nir Gov for helpful discussions.

## References

- [1] Betz T, Lenz M, Joanny J and Sykes C 2009 ATP-dependent mechanics of red blood cells *Proc. Natl Acad. Sci. USA* **106** 15320–5
- [2] Sunyer R, Ritort F, Farre R and Navajas D 2009 Thermal activation and ATP dependence of the cytoskeleton remodeling dynamics *Phys. Rev. E* **79** 051920
- [3] Parry B, Surovtsev I, Cabeen M, O'Hern C, Dufresne E and Jacobs-Wagner C 2014 The bacterial cytoplasm has glass-like properties and is fluidized by metabolic activity *Cell* **156** 183–94
- [4] Girard P, Prost J and Bassereau P 2005 Passive or active fluctuations in membranes containing proteins *Phys. Rev. Lett.* **94** 088102
- [5] Faris M, Lacoste D, Pecreaux J, Joanny J, Prost J and Bassereau P 2009 Membrane tension lowering induced by protein activity *Phys. Rev. Lett.* **102** 038102
- [6] Weber S, Spakowitz A and Theriot J 2012 Nonthermal ATP-dependent fluctuations contribute to the *in vivo* motion of chromosomal loci *Proc. Natl Acad. Sci. USA* **109** 7338–43
- [7] Hameed F, Rao M and Shivashankar G 2012 Dynamics of passive and active particles in the cell nucleus *PLoS One* **7** e45843
- [8] MacKintosh F C and Schmidt C F 2010 Active cellular materials *Curr. Opin. Cell Biol.* **22** 29–35
- [9] Brangwynne C P, Koenderink G H, MacKintosh F C and Weitz D A 2008 Cytoplasmic diffusion: molecular motors mix it up *J. Cell Biol.* **183** 583–7
- [10] Gal N, Lechtman-Goldstein D and Weihs D 2013 Particle tracking in living cells: a review of the mean square displacement method and beyond *Rheol. Acta* **5** 425–43
- [11] Waigh T 2005 Microrheology of complex fluids *Rep. Prog. Phys.* **68** 685–742
- [12] Wirtz D 2009 Particle-tracking microrheology of living cells: principles and applications *Annu. Rev. Biophys.* **38** 301–26
- [13] Hoffman B D, Massiera G, Van Citters K M and Crocker J C 2006 The consensus mechanics of cultured mammalian cells *Proc. Natl Acad. Sci. USA* **103** 10259–64
- [14] Robert D, Aubertin K, Bacri J and Wilhelm C 2012 Magnetic nanomanipulations inside living cells compared with passive tracking of nanoprobe to get consensus for intracellular mechanics *Phys. Rev. E* **85** 011905
- [15] Squires T and Mason T 2010 Fluid mechanics of microrheology *Annu. Rev. Fluid Mech.* **42** 413–38
- [16] Wilson L and Poon W 2011 Small-world rheology: an introduction to probe-based active microrheology *Phys. Chem. Chem. Phys.* **13** 10617–30
- [17] Mason T and Weitz D 1995 Optical measurements of frequency-dependent linear viscoelastic moduli of complex fluids *Phys. Rev. Lett.* **74** 1250–3
- [18] Gittes F, Schnurr B, Olmsted P, MacKintosh F and Schmidt C 1997 Microscopic viscoelasticity: shear moduli of soft materials determined from thermal fluctuations *Phys. Rev. Lett.* **79** 3286–9
- [19] Chaikin P and Lubensky T 1995 *Principles of Condensed Matter Physics* (Cambridge: Cambridge University Press)
- [20] Einstein A 1905 Über die von der molekularkinetischen Theorie der Wärme geforderte Bewegung von in ruhenden Flüssigkeiten suspendierten Teilchen *Ann. Phys., Lpz.* **17** 549–60



- [21] Lau A, Hoffman B, Davies A, Crocker J and Lubensky T 2003 Microrheology, stress fluctuations, and active behavior of living cells *Phys. Rev. Lett.* **91** 198101
- [22] Wilhelm C 2008 Out-of-equilibrium microrheology inside living cells *Phys. Rev. Lett.* **101** 028101
- [23] Gallet F, Arcizet D, Bohec P and Richert A 2009 Power spectrum of out-of-equilibrium forces in living cells: amplitude and frequency dependence *Soft Matter* **5** 2947–53
- [24] Robert D, Nguyen T, Gallet F and Wilhelm C 2010 *In vivo* determination of fluctuating forces during endosome trafficking using a combination of active and passive microrheology *PLoS One* **5** e10046
- [25] Bohec P, Gallet F, Maes C, Safaverdi S, Visco P and van Wijland F 2013 Probing active forces via a fluctuation–dissipation relation: application to living cells *Europhys. Lett.* **102** 50005
- [26] Caspi A, Granek R and Elbaum M 2000 Enhanced diffusion in active intracellular transport *Phys. Rev. Lett.* **85** 5655–8
- [27] Massiera G, Van Citters K, Biancaniello P and Crocker J 2007 Mechanics of single cells: rheology, time dependence, and fluctuations *Biophys. J.* **93** 3703–13
- [28] Arcizet D, Meier B, Sackmann E, Rädler J O and Heinrich D 2008 Temporal analysis of active and passive transport in living cells *Phys. Rev. Lett.* **101** 248103
- [29] Jeon J H, Tejedor V, Burov S, Barkai E, Selhuber-Unkel C, Berg-Sørensen K, Oddershede L and Metzler R 2011 *In vivo* anomalous diffusion and weak ergodicity breaking of lipid granules *Phys. Rev. Lett.* **106** 048103
- [30] Hale C, Sun S and Wirtz D 2009 Resolving the role of actomyosin contractility in cell microrheology *PLoS One* **4** e7054
- [31] Goldstein D, Elhanan T, Aronovitch M and Weihs M 2013 Origin of active transport in breast-cancer cells *Soft Matter* **9** 7167–73
- [32] Head D A and Mizuno D 2010 Nonlocal fluctuation correlations in active gels *Phys. Rev. E* **81** 041910
- [33] Mizuno D, Tardin C, Schmidt C F and MacKintosh F C 2007 Nonequilibrium mechanics of active cytoskeletal networks *Science* **315** 370–3
- [34] Mizuno D, Head D, MacKintosh F and Schmidt C 2008 Active and passive microrheology in equilibrium and nonequilibrium systems *Macromolecules* **41** 7194–202
- [35] Toyota T, Head D A, Schmidt C F and Mizuno D 2011 Non-Gaussian athermal fluctuations in active gels *Soft Matter* **7** 3234–9
- [36] Brangwynne C P, Koenderink G H, Mackintosh F C and Weitz D A 2008 Nonequilibrium microtubule fluctuations in a model cytoskeleton *Phys. Rev. Lett.* **100** 118104
- [37] Sanchez T, Chen D, DeCamp S, Heymann M and Dogic Z 2012 Spontaneous motion in hierarchically assembled active matter *Nature* **491** 431–4
- [38] Finer J, Simmons R and Spudich J 1994 Single myosin molecule mechanics: piconewton forces and nanometre steps *Nature* **368** 113–9
- [39] LeGoff L, Amblard F and Furst E 2002 Motor-driven dynamics in actin–myosin networks *Phys. Rev. Lett.* **88** 018101
- [40] Bendix P M, Koenderink G H, Cuvelier D, Dogic Z, Koeleman B N, Briehner W M, Field C M, Mahadevan L and Weitz D A 2008 A quantitative analysis of contractility in active cytoskeletal protein networks *Biophys. J.* **94** 3126–36
- [41] Soares e Silva M, Depken M, Stuhmann B, Korsten M, MacKintosh F C and Koenderink G H 2011 Active multistage coarsening of actin networks driven by myosin motors *Proc. Natl Acad. Sci. USA* **108** 9408–13
- [42] Köhler S and Bausch A 2012 Contraction mechanisms in composite active actin networks *PLoS One* **7** e39869
- [43] Köhler S, Schmoller K, Crevenna A and Bausch A 2012 Regulating contractility of the actomyosin cytoskeleton by pH *Cell Rep.* **2** 433–9
- [44] Valentine M T, Kaplan P D, Thota D, Crocker J C, Gisler T, Prud’Homme R K, Beck M and Weitz D A 2001 Investigating the microenvironments of inhomogeneous soft materials with multiple particle tracking *Phys. Rev. E* **64** 061506

- [45] Ben-Isaac E, Park Y, Popescu G, Brown F, Gov N and Shokef Y 2011 Effective temperature of red-blood-cell membrane fluctuations *Phys. Rev. Lett.* **106** 238103
- [46] Koenderink G H, Dogic Z, Nakamura F, Bendix P M, MacKintosh F C, Hartwig J H, Stossel T P and Weitz D A 2009 An active biopolymer network controlled by molecular motors *Proc. Natl Acad. Sci. USA* **106** 15192–7
- [47] Bertrand O, Fygenson D and Saleh O 2012 Active, motor-driven mechanics in a DNA gel *Proc. Natl Acad. Sci. USA* **109** 17342–7
- [48] MacKintosh F C and Levine A J 2008 Nonequilibrium mechanics and dynamics of motor-activated gels *Phys. Rev. Lett.* **100** 018104
- [49] Morozov K and Pismen L 2010 Motor-driven effective temperature and viscoelastic response of active matter *Phys. Rev. E* **81** 061922
- [50] Levine A and MacKintosh F 2009 The mechanics and fluctuation spectrum of active gels *J. Phys. Chem. B* **113** 3820–30
- [51] Erdmann T and Schwarz U 2012 Stochastic force generation by small ensembles of myosin II motors *Phys. Rev. Lett.* **108** 188101
- [52] Backouche F, Haviv L, Groswasser D and Bernheim-Groswasser A 2006 Active gels: dynamics of patterning and self-organization *Phys. Biol.* **3** 264–73
- [53] Gordon D, Bernheim-Groswasser A, Keasar C and Farago O 2012 Hierarchical self-organization of cytoskeletal active networks *Phys. Biol.* **9** 026005
- [54] Alvarado J, Sheinman M, Sharma A, MacKintosh F and Koenderink G 2013 Molecular motors robustly drive active gels to a critically connected state *Nat. Phys.* **9** 591–7
- [55] Smith D, Ziebert F, Humphrey D, Duggan C, Steinbeck M, Zimmermann W and Käs J 2007 Molecular motor-induced instabilities and cross linkers determine biopolymer organization *Biophys. J.* **93** 4445–52
- [56] Stuhmann B, Soares M, Depken M, MacKintosh F and Koenderink G 2012 Nonequilibrium fluctuations of a remodeling *in vitro* cytoskeleton *Phys. Rev. E* **86** 020901
- [57] Pardee J D and Spudich J A 1982 Purification of muscle actin *Methods Enzymology* **85** 164–81
- [58] Crocker J C and Grier D G 1996 Methods of digital video microscopy for colloidal studies *J. Colloid Interface Sci.* **179** 298–310
- [59] Kron S J and Spudich J A 1986 Fluorescent actin filaments move on myosin fixed to a glass surface *Proc. Natl Acad. Sci. USA* **83** 6272–6
- [60] Köhler S, Schaller V and Bausch A 2011 Structure formation in active networks *Nat. Mater.* **10** 462–8
- [61] Köhler S, Schaller V and Bausch A 2011 Collective dynamics of active cytoskeletal networks *PLoS One* **6** e23798
- [62] Ideses Y, Sonn-Segev A, Roichman Y and Bernheim-Groswasser A 2013 Myosin II does it all: assembly, remodeling, and disassembly of actin networks are governed by myosin II activity *Soft Matter* **9** 7127–37
- [63] Humphrey D, Duggan C, Saha D, Smith D and Käs J 2002 Active fluidization of polymer networks through molecular motors *Nature* **416** 413–6
- [64] Rauzi M, Lenne P and Lecuit T 2010 Planar polarized actomyosin contractile flows control epithelial junction remodelling *Nature* **468** 1110–4